$\dot{R}_{out}\, T_d (T_{out}^{-1} - T_{in}^{-1})$, where $\dot{R}_{out}$ is the outgoing long-wave radiation and T_{in}, T_{out}, and T_d are the mean temperature of atmospheric heat input, output, and dissipation, respectively. Observations of recent tropospheric warming [figures 2.26 and 2.27 in (*32*)] show that temperature trends are somewhat uniform in the vertical, which suggests that the difference $T_{out}^{-1} - T_{in}^{-1}$ might increase more slowly than either T_{in} or T_{out}. This slower increase may explain why $\delta \dot{Q}_{total}$ does not follow a surface Clausius-Clapeyron scaling and why one would expect moist processes to limit the work output in simulations with anthropogenic forcing. Simulations over a wider range of climates would help verify this hypothesis.

Our comparison of thermodynamic cycles in CESM and MERRA show many similarities; however, we find that CESM requires less power to maintain its hydrological cycle than the reanalysis, due to the smaller amplitude of its moistening inefficiencies. We suggest that this difference might be a consequence of the idealized nature of parameterized convection schemes, and it is likely that it might also influence the response of CESM to anthropogenic forcing. Typically, convection schemes artificially transport moisture along a moist adiabat without accounting for the work needed to lift this moisture, but in the real world, this work is necessary to sustain precipitation. Any increase in global precipitation therefore requires an increase in work output; otherwise, precipitation would have to become more efficient, for example, by reducing the frictional dissipation of falling hydrometeors (*11*, *12*). This is one reason we should interpret the constraint in work output in CESM as a constraint on the large-scale motions and not on the unresolved subgrid-scale convective events.

Our work illustrates a major constraint on the large-scale global atmospheric engine: As the climate warms, the system may be unable to increase its total entropy production enough to offset the moistening inefficiencies associated with phase transitions. This suggests that in a future climate, the global atmospheric circulation might comprise highly energetic storms due to explosive latent heat release, but in such a case, the constraint on work output identified here will result in fewer numbers of such events. Earth's atmospheric circulation thus suffers from the "water in gas problem" observed in simulations of tropical convection (*6*), where its ability to produce work is constrained by the need to convert liquid water into water vapor and back again to tap its fuel.

REFERENCES AND NOTES

1. L. Barry, G. C. Craig, J. Thuburn, *Nature* **415**, 774–777 (2002).
2. M. H. P. Ambaum, *Thermal Physics of the Atmosphere* (Wiley, Hoboken, 2010), pp. 203–220.
3. O. R. Wulf, L. Davis Jr., *J. Meteorol.* **9**, 80–82 (1952).
4. J. P. Peixoto, A. H. Oort, M. De Almeida, A. Tomé, *J. Geophys. Res.* **96** (D6), 10981 (1991).
5. R. Goody, *Q. J. R. Meteorol. Soc.* **126**, 1953–1970 (2000).
6. O. Pauluis, I. M. Held, *J. Atmos. Sci.* **59**, 125–139 (2002).
7. D. M. Romps, *J. Atmos. Sci.* **65**, 3779–3799 (2008).
8. S. Pascale, J. Gregory, M. Ambaum, R. Tailleux, *Clim. Dyn.* **36**, 1189–1206 (2011).
9. O. Pauluis, I. M. Held, *J. Atmos. Sci.* **59**, 140–149 (2002).
10. O. Pauluis, *J. Atmos. Sci.* **68**, 91–102 (2011).
11. O. Pauluis, V. Balaji, I. M. Held, *J. Atmos. Sci.* **57**, 989–994 (2000).
12. O. Pauluis, J. Dias, *Science* **335**, 953–956 (2012).
13. S. Sherwood, R. Roca, T. Weckwerth, N. Andronova, *Rev. Geophys.* **48**, RG2001 (2010).
14. I. Held, B. Soden, *J. Clim.* **19**, 5686–5699 (2006).
15. R. Caballero, P. L. Langen, *Geophys. Res. Lett.* **32**, L02705 (2005).
16. P. O'Gorman, T. Schneider, *J. Clim.* **21**, 5797–5806 (2008).
17. T. Schneider, P. A. O'Gorman, X. Levine, *Rev. Geophys.* **48**, RG3001 (2010).
18. G. Vecchi, B. Soden, *J. Clim.* **20**, 4316–4340 (2007).
19. R. Feistel *et al.*, *Ocean Science* **6**, 91–141 (2010).
20. Materials and methods are available as supplementary material on *Science* Online.
21. K. Emanuel, *Atmospheric Convection* (Oxford Univ. Press, MIT, Oxford, 1994).
22. D. R. Johnson, *International Geophysics*, D. A. Randall, Ed. (Academic Press, Waltham, 2001), pp. 659–720.
23. P. R. Gent *et al.*, *J. Clim.* **24**, 4973–4991 (2011).
24. R. H. Moss *et al.*, *Nature* **463**, 747–756 (2010).
25. M. M. Rienecker *et al.*, *J. Clim.* **24**, 3624–3648 (2011).
26. J. D. Zika, M. H. England, W. P. Sijp, *J. Phys. Oceanogr.* **42**, 708–724 (2012).
27. K. Döös, J. Nilsson, J. Nycander, L. Brodeau, M. Ballarotta, *J. Phys. Oceanogr.* **42**, 1445–1460 (2012).
28. J. Kjellsson, K. Döös, F. B. Laliberté, J. D. Zika, *J. Atmos. Sci.* **71**, 916–928 (2014).
29. S. Groeskamp, J. D. Zika, T. J. McDougall, B. M. Sloyan, F. Laliberté, *J. Phys. Oceanogr.* **44**, 1735–1750 (2014).
30. O. M. Pauluis, A. A. Mrowiec, *J. Atmos. Sci.* **70**, 3673–3688 (2013).
31. V. Lucarini, K. Fraedrich, F. Ragone, *J. Atmos. Sci.* **68**, 2438–2458 (2011).
32. D. L. Hartmann *et al.*, Climate Change 2013: The Physical Science Basis. Contribution of Working Group I to the Fifth Assessment Report of the Intergovernmental Panel on Climate Change, T. F. Stocker *et al.*, Eds. (Cambridge Univ. Press, Cambridge and New York, NY, USA, 2013).

ACKNOWLEDGMENTS

We acknowledge the Global Modeling and Assimilation Office (GMAO) and the Goddard Earth Sciences Data and Information Services Center (GES DISC) for the dissemination of MERRA data. This work was supported by the G8 Research Initiative grant "ExArch: Climate analytics on distributed exascale data archives" made available through the Natural Sciences and Engineering Research Council (NSERC).

SUPPLEMENTARY MATERIALS

www.sciencemag.org/content/347/6221/540/suppl/DC1
Materials and Methods
Supplementary Text
Figs. S1 to S5
References (*33*–*36*)

9 June 2014; accepted 3 December 2014
10.1126/science.1257103

OPTICAL IMAGING

Expansion microscopy

Fei Chen,[1]* Paul W. Tillberg,[2]* Edward S. Boyden[1,3,4,5,6]†

In optical microscopy, fine structural details are resolved by using refraction to magnify images of a specimen. We discovered that by synthesizing a swellable polymer network within a specimen, it can be physically expanded, resulting in physical magnification. By covalently anchoring specific labels located within the specimen directly to the polymer network, labels spaced closer than the optical diffraction limit can be isotropically separated and optically resolved, a process we call expansion microscopy (ExM). Thus, this process can be used to perform scalable superresolution microscopy with diffraction-limited microscopes. We demonstrate ExM with apparent ~70-nanometer lateral resolution in both cultured cells and brain tissue, performing three-color superresolution imaging of ~10^7 cubic micrometers of the mouse hippocampus with a conventional confocal microscope.

Microscopy has facilitated the discovery of many biological insights by optically magnifying images of structures in fixed cells and tissues. We here report that physical magnification of the specimen itself is also possible.

We first set out to see whether a well-known property of polyelectrolyte gels—namely, that dialyzing them in water causes expansion of the polymer network into extended conformations (Fig. 1A) (*1*)—could be performed in a biological sample. We infused into chemically fixed and permeabilized brain tissue (Fig. 1B) sodium acrylate, a monomer used to produce superabsorbent materials (*2*, *3*), along with the comonomer acrylamide and the cross-linker N-N′-methylenebisacrylamide. After triggering free radical polymerization with ammonium persulfate (APS) initiator and tetramethylethylenediamine (TEMED) accelerator, we treated the tissue-polymer composite with protease to homogenize its mechanical characteristics. After proteolysis, dialysis in water resulted in a 4.5-fold linear expansion, without distortion at the level of gross anatomy (Fig. 1C). Digestion was uniform throughout the slice (fig. S1). Expanded specimens were transparent (fig. S2) because they consist largely of water. Thus, polyelectrolyte gel expansion is possible when the polymer is embedded throughout a biological sample.

We developed a fluorescent labeling strategy compatible with the proteolytic treatment and subsequent tissue expansion described above,

[1]Department of Biological Engineering, Massachussetts Institute of Technology (MIT), Cambridge, MA, USA. [2]Department of Electrical Engineering and Computer Science, MIT, Cambridge, MA, USA. [3]Media Lab, MIT, Cambridge, MA, USA. [4]McGovern Institute, MIT, Cambridge, MA, USA. [5]Department of Brain and Cognitive Sciences, MIT, Cambridge, MA, USA. [6]Center for Neurobiological Engineering, MIT, Cambridge, MA, USA.
*These authors contributed equally to this work. **†Corresponding author. E-mail: esb@media.mit.edu**

Downloaded from https://www.science.org on March 15, 2025

IPR2024-00526
EX 1085

to see whether fluorescence nanoscopy would be possible. We designed a custom fluorescent label (Fig. 1D) that can be incorporated directly into the polymer network and thus survives the proteolytic digestion of endogenous biomolecules. This label is trifunctional, comprising a methacryloyl group capable of participating in free radical polymerization, a chemical fluorophore for visualization, and an oligonucleotide that can hybridize to a complementary sequence attached to an affinity tag (such as a secondary antibody) (Fig. 1, E and F). Thus, the fluorescent tag is targeted to a biomolecule of interest yet remains anchored covalently with high yield (table S1) to the polymer network. The entire process of labeling, gelation, digestion, expansion, and imaging we call expansion microscopy (ExM).

We performed fluorescence imaging using ExM, examining microtubules in fixed human embryonic kidney (HEK) 293 cells labeled with the trifunctional label and imaged with confocal laser scanning microscopy pre- versus post-ExM processing. The post-ExM image (Fig. 2B) was registered to the pre-ExM image (Fig. 2A) via a similarity transformation, resulting in visually indistinguishable images. To quantify the isotropy of ExM, we calculated the deformation vector field between the images via a nonrigid registration process (fig. S3). From this vector field, we quantified the root-mean-square (RMS) error of feature measurements post-ExM. The errors in length were small (<1% of distance, for errors larger than the imaging system point spread function size; n = 4 samples) (Fig. 2C). Throughout the paper, all distances measured in the post-expansion specimen are reported divided by the expansion factor (supplementary materials, materials and methods).

We next compared pre-ExM conventional superresolution images to post-ExM confocal images. We labeled features traditionally used to characterize the performance of superresolution microscopes, including microtubules (*4*, *5*) and clathrin coated pits (*6*), and imaged them with a superresolution structured illumination microscope (SR-SIM) pre-ExM, and a spinning disk confocal post-ExM. Qualitatively (Fig. 2, D and E), the images were similar, and quantitatively (Fig. 2I), measurement errors were again on the order of 1% and well within the point spread function size of the SR-SIM microscope (n = 4 samples). Microtubule networks were more sharply resolved in ExM (Fig. 2G) than with SR-SIM (Fig. 2F). ExM resolved individual microtubules that could not be distinguished with SR-SIM (Fig. 2H). Microtubules imaged with ExM presented a full-width at half-maximum (FWHM) (Fig. 2J) of 83.8 ± 5.68 nm (mean ± SD, n = 24 microtubules from 3 samples). This FWHM reflects the effective resolution of ExM convolved by the width of the labeled microtubule. To estimate the effective resolution of ExM, we deconvolved [as in (*7*)] our observed microtubule FWHM by the known immunostained microtubule width [55 nm (*6*)], conservatively ignoring the width of the trifunctional label, and obtained an effective resolution for ExM of ~60 nm. This conservative estimate is comparable with the diffraction-limited confocal resolution [~250-nm lateral resolution (*8*)] divided by the expansion factor (~4.5).

Clathrin-coated pits were also well resolved (Fig. 2, K and L). ExM resolved the central nulls of the pits better than SR-SIM (Fig. 2, M and N). Clathrin-coated pit radii measured via ExM and SR-SIM were highly correlated, with a slope of 1.001 (total least squares regression, confidence interval 0.013 with P <0.05, n = 50 pits from three samples) (Fig. 2O). Forty-nine of the 50 points lay within a half-pixel distance of the unity slope line, suggesting that variation in the ExM versus SR-SIM comparison was within the digitization error of the measurement.

We next applied ExM to fixed brain tissue. Slices of brain from Thy1-YFP-H mice expressing cytosolic yellow fluorescent protein (YFP) under the Thy1 promoter in a subset of neurons (*9*) were stained with a trifunctional label bearing Alexa 488, using primary antibodies to green fluorescent protein (GFP) (which also bind YFP). Slices expanded fourfold, similar to the expansion factor in cultured cells. We compared pre- versus post-ExM images taken on an epifluorescence microscope. As with cultured cells, the post-ExM image (Fig. 3B) was registered to the pre-ExM

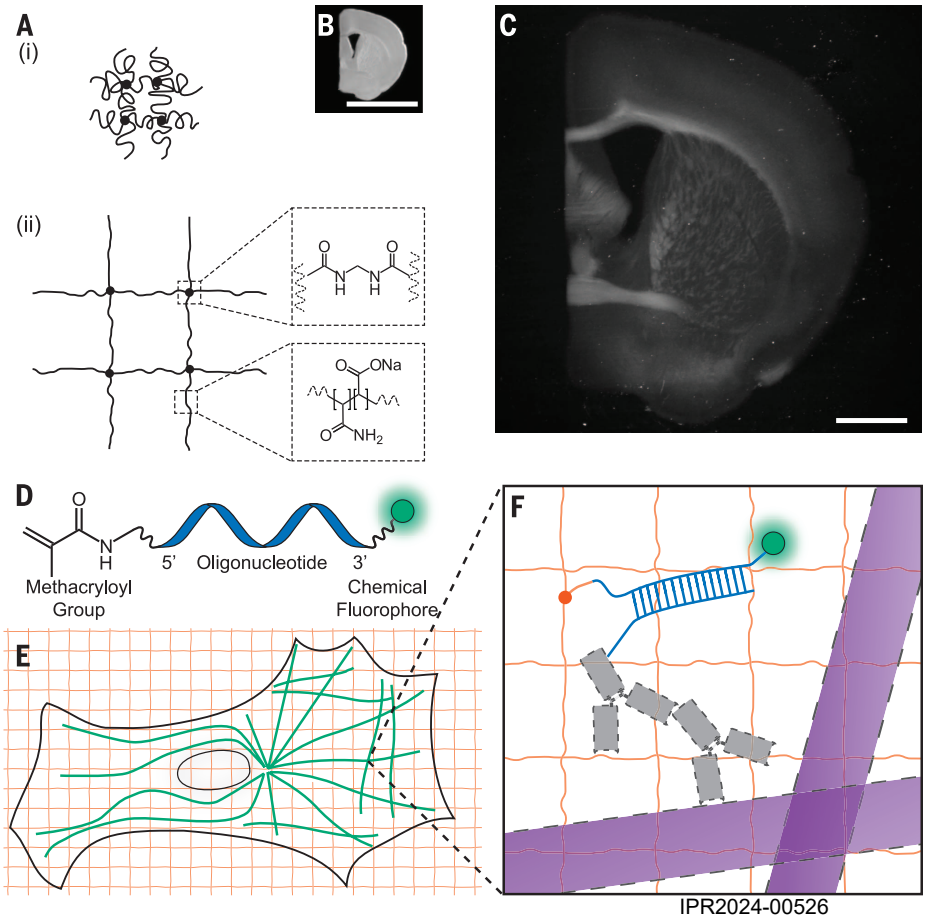

Fig. 1. Expansion microscopy (ExM) concept. (**A**) Schematic of (i) collapsed polyelectrolyte network, showing crosslinker (dot) and polymer chain (line), and (ii) expanded network after H_2O dialysis. (**B**) Photograph of fixed mouse brain slice. (**C**) Photograph, post-ExM, of the sample (B) under side illumination. (**D**) Schematic of label that can be anchored to the gel at site of a biomolecule. (**E**) Schematic of microtubules (green) and polymer network (orange). (**F**) The label of (D), hybridized to the oligo-bearing secondary antibody top (top gray shape) bound via the primary (bottom gray shape) to microtubules (purple), is incorporated into the gel (orange lines) via the methacryloyl group (orange dot) and remains after proteolysis (dotted lines). Scale bars, (B) and (C) 5 mm. Schematics are not to scale.

Downloaded from https://www.science.org on March 15, 2025

IPR2024-00526
EX 1085

image (Fig. 3A) via a similarity transformation. The registered images closely matched, although some features moved in or out of the depth of field because of the axial expansion post-ExM. Quantitatively, post-ExM measurement errors (Fig. 3C, n = 4 cortical slices) were 2 to 4%.

We synthesized trifunctional labels with different colors and oligonucleotides (supplementary materials, materials and methods) to enable multicolor ExM. We obtained pre- (Fig. 3D) versus post-ExM (Fig. 3E) images of Thy1-YFP-H mouse cortex with ExM labels directed against YFP (Fig. 3E, green) and the pre- and postsynaptic scaffolding proteins Bassoon (Fig. 3E, blue) and Homer1 (Fig. 3E, red). In the pre-ExM image, Bassoon and Homer1 staining form overlapping spots at each synapse (Fig. 3F), whereas the post-ExM image (Fig. 3G) shows clearly distinguishable pre- and postsynaptic labeling. We quantified the distance between the Bassoon and Homer1 scaffolds, as measured with ExM. We fit the distributions of Bassoon and Homer1 staining intensity, taken along the line perpendicular to the synaptic cleft (Fig. 3H, boxed region), to Gaussians (Fig. 3I). The Bassoon-Homer1 separation was 169 ± 32.6 nm (Fig. 3J, n = 277 synapses from four cortical slices), similar to a previous study using stochastic optical reconstruction microscopy (STORM) in the ventral cortex and olfactory bulb, which obtained ~150 nm

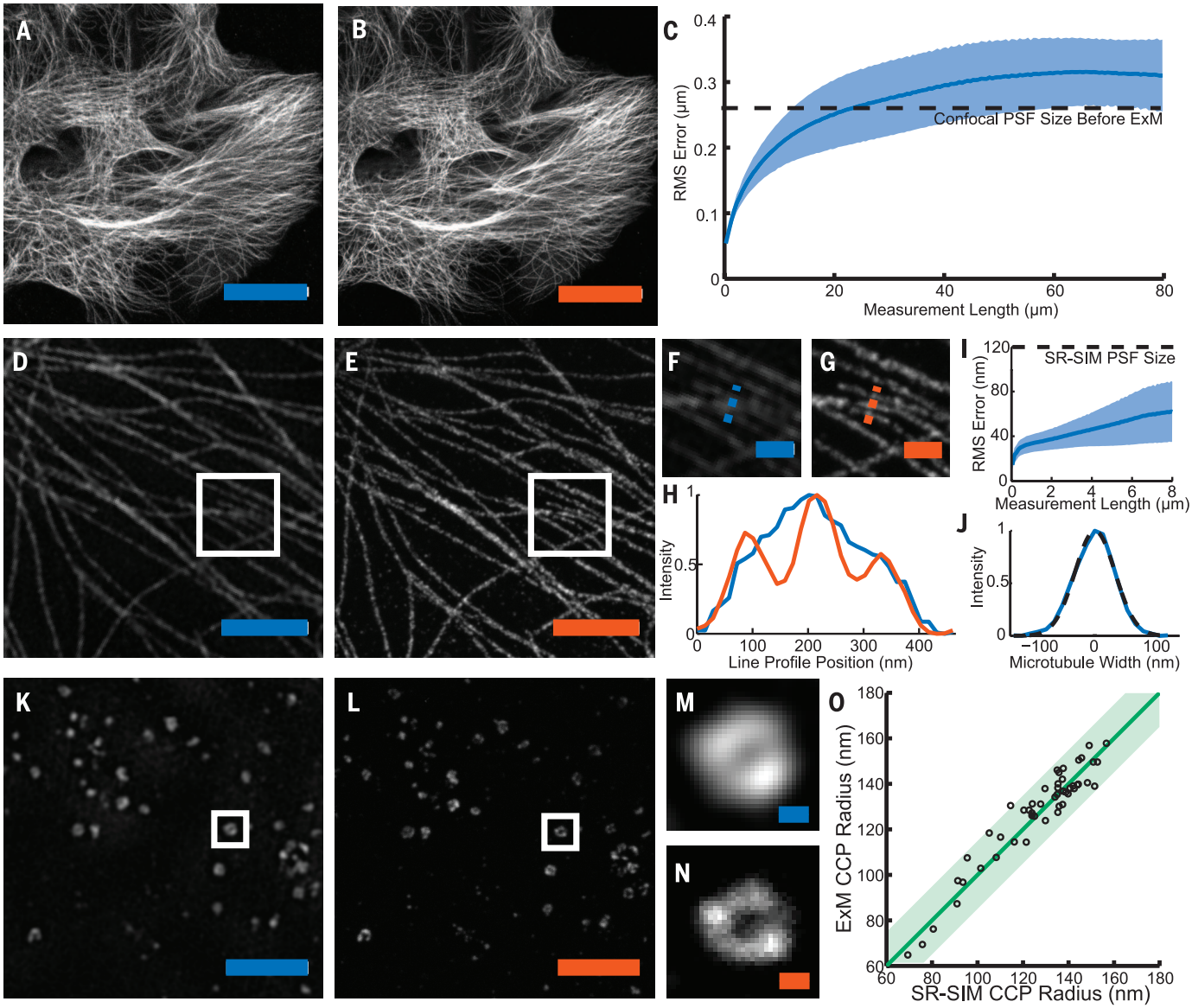

Fig. 2. Expansion microscopy physically magnifies, with nanoscale isotropy. We compared images acquired via conventional microscopy (blue scale bars) versus images acquired post-expansion (orange scale bars). (**A**) Confocal image of microtubules in HEK293 cells. (**B**) Post-expansion confocal image of sample (A). (**C**) RMS length measurement error of pre- versus post-ExM confocal images of cultured cells (blue line, mean; shaded area, standard deviation; n = 4 samples). (**D**) SR-SIM image of microtubules. (**E**) Post-expansion confocal image of the sample of (D). (**F** and **G**) Magnified views of boxed regions of (D) and (E), respectively. (**H**) Profiles of microtubule intensity taken along the blue and orange dotted lines in (F) and (G). (**I**) RMS length measurement error of ExM versus SR-SIM images (blue line, mean; shaded area, standard deviation; n = 4 samples). (**J**) Transverse profile of a representative microtubule (blue line), with Gaussian fit (black dotted line). (**K**) SR-SIM image of clathrin-coated pits (CCPs) in HEK293 cells. (**L**) Post-expansion confocal image of the sample of (K). (**M** and **N**) Magnified views of a single CCP in the boxed regions of (K) and (L), respectively. (**O**) Scatterplot of radii of CCPs measured via ExM versus SR-SIM (n = 50 CCPs from 3 samples). Green line, $y = x$ line; shaded green region, half-pixel width of digitization error about the $y = x$ line. Scale bars for pre- versus post-ExM images, (A) 20 μm; (B) 20 μm (physical size post-expansion, 81.6 μm); (D) 2 μm; (E) 2 μm (9.1 μm); (F) 500 nm; (G) 500 nm (2.27 μm); (K) 2 μm; (L) 2 μm (8.82 μm); (M) 100 nm; (N) 100 nm (441 nm).

IPR2024-00526
EX 1085

Downloaded from https://www.science.org on March 15, 2025

separation (*10*). We also imaged other antibody targets of interest in biology (fig. S4).

To explore whether expanded samples, scanned on fast diffraction-limited microscopes, could support scalable superresolution imaging, we imaged a volume of the adult Thy1-YFP-H mouse brain spanning 500 by 180 by 100 μm (tissue slice thickness), with three labels (antibody to GFP, green; antibody to Homer1, red; antibody to Bassoon, blue) (Fig. 4A). The diffraction limit of our confocal spinning disk microscope (with 40×, 1.15 NA, water immersion objective), divided by the expansion factor, yields an estimated effective resolution of ~70 nm laterally and ~200 nm axially. Shown in Fig. 4A is a three-dimensional (3D) rendered image of the data set (an animated rendering is provided in movie S1). Zooming into the raw data set, nanoscale features emerge (Fig. 4, B to D). We performed a volume rendering of the YFP-expressing neurons in a subset of CA1 stratum lacunosum moleculare (slm), revealing spine morphology (Fig. 4B and movie S2). Focusing on a dendrite in CA1 slm, we observed the postsynaptic protein Homer1

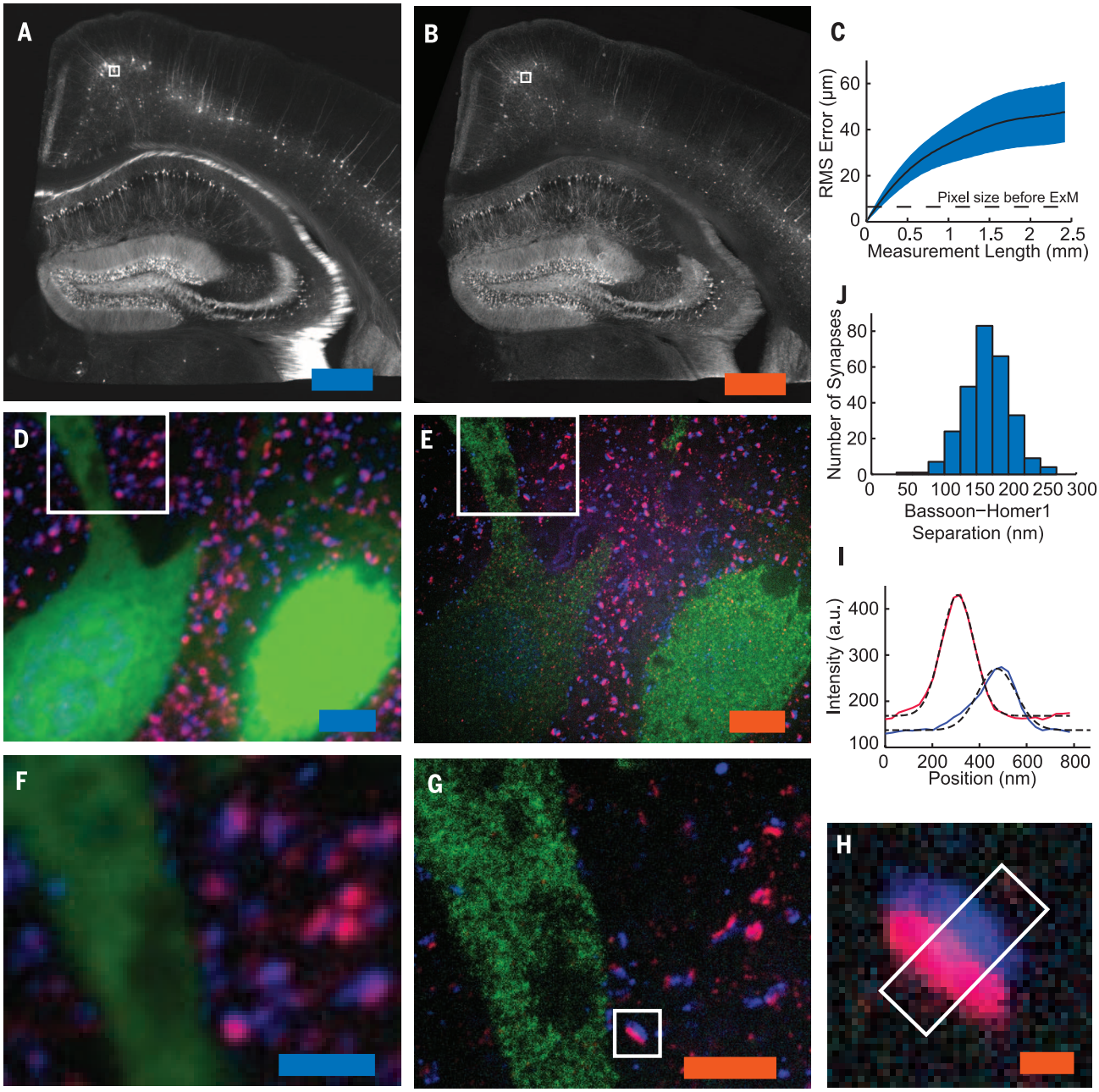

Fig. 3. ExM imaging of mammalian brain tissue. (**A**) Widefield fluorescence (white) image of Thy1-YFP mouse brain slice. (**B**) Post-expansion widefield image of sample (A). (**C**) RMS length measurement error for pre- versus post-ExM images of brain slices (blue line, mean; shaded area, SD; $n = 4$ samples). (**D** and **E**) Confocal fluorescence images of boxed regions in (A) and (B), respectively, stained with presynaptic (anti-Bassoon, blue) and postsynaptic (anti-Homer1, red) markers, in addition to antibody to GFP (green), pre- (D) versus post- (E) expansion. (**F** and **G**) Details of boxed regions in (D) and (E), respectively. (**H**) Single representative synapse highlighted in (G). (**I**) Staining intensity for Bassoon (blue) and Homer1 (red) of the sample of (H) along white box long axis. Dotted black lines, Gaussian fits. a.u., arbitrary units. (**J**) Bassoon-Homer1 separation ($n = 277$ synapses from four cortical slices). Scale bars for pre- versus post-ExM images, (A) 500 μm; (B) 500 μm (physical size post-expansion 2.01 mm); (D) 5 μm; (E) 5 μm (20.1 μm); (F) 2.5 μm; (G) 2.5 μm (10.0 μm); and (H) 250 nm (1.00 μm).

IPR2024-00526
EX 1085

Downloaded from https://www.science.org on March 15, 2025

to be well localized to dendritic spine heads, with the presynaptic molecule Bassoon in apposition (Fig. 4C and movie S3). Examination of a mossy fiber bouton in the hilus of the dentate gyrus reveals invaginations into the bouton by spiny excrescences of the opposing dendrite, as observed previously via electron microscopy (Fig. 4D) (*11*). Thus, ExM enables multiscale imaging and visualization of nanoscale features, across length scales relevant to understanding neural circuits.

We report the discovery of a new modality of magnification, namely that fixed cells and tissues, appropriately labeled and processed, can be physically magnified, with isotropic nanoscale resolution (effective ~60-nm lateral resolution). Although acrylate esters have been used for antigen-preserving embedding for electron microscopy (*12*, *13*), ExM represents the first use of an embedded polyelectrolyte gel, used here to expand the specimen. Superresolution imaging methods are slower than their diffraction-limited counterparts because they must resolve more voxels per unit volume. ExM achieves this by expanding the voxels physically. ExM achieves the same voxel throughputs as a diffraction-limited microscope, but at the voxel sizes of a superresolution microscope. Ongoing technology trends for faster diffraction-limited microscopy (*14*) will continue to boost ExM speed.

The physical magnification of ExM enables superresolution imaging with several fundamental new properties. The axial effective resolution is improved by the same factor as the lateral effective resolution. ExM can achieve superresolution with standard fluorophores, and on a diffraction-limited microscope. Superresolution imaging is often performed within ~10 μm of the sample surface because of low signal-to-noise, scattering, and refractive index mismatch. We were able to perform three-color superresolution imaging of a large volume of brain tissue over an axial extent of 100 μm with a spinning disk confocal microscope. Because the ExM-processed sample is almost entirely water, eliminating scattering, ExM may empower fast methods such as light-sheet microscopy (*15*) to become superresolution methods. ExM potentially enables labels to be situated within a well-defined, in vitro–like environment, facilitating in situ analysis (*16*). Because the

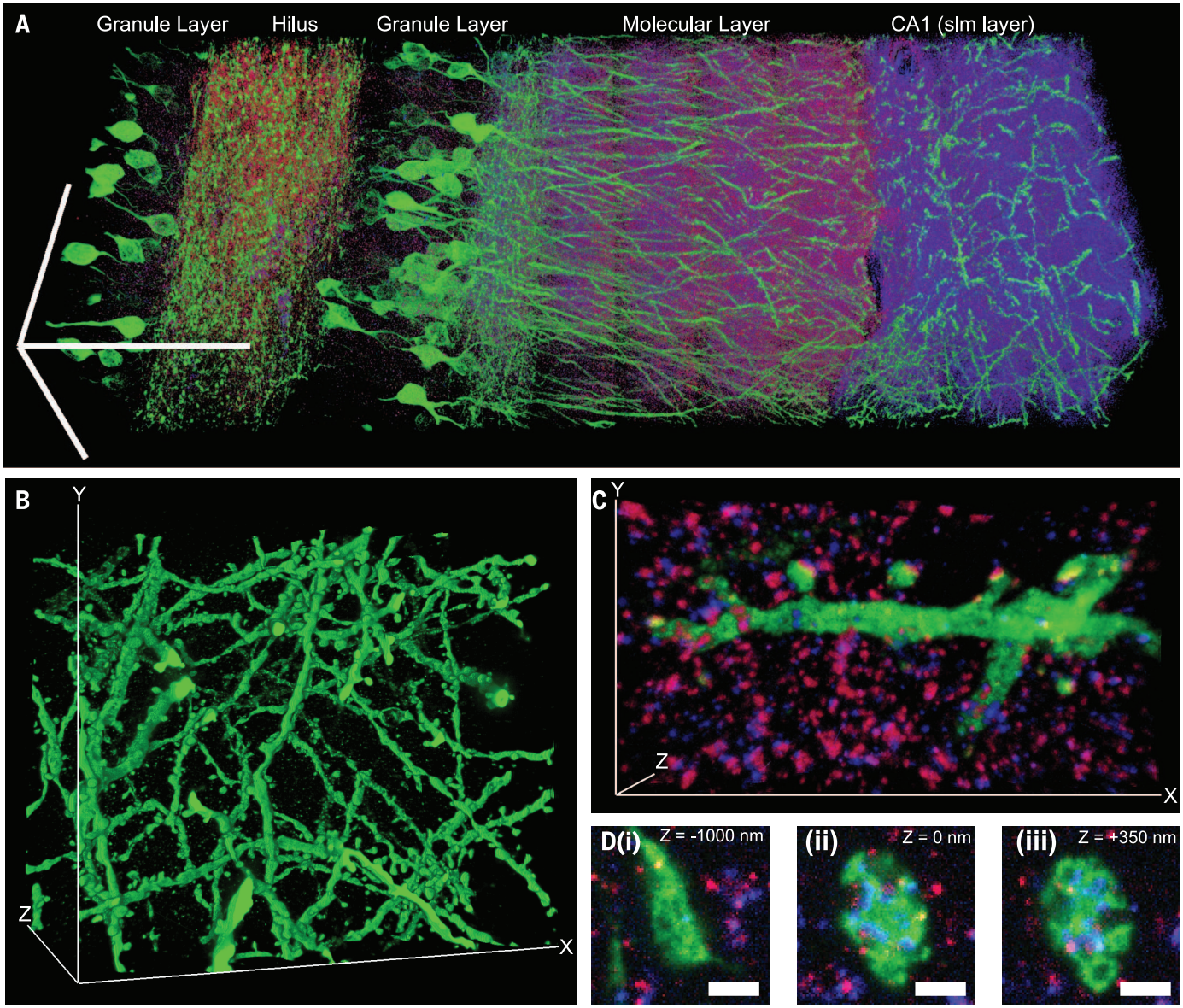

Fig. 4. Scalable 3D superresolution microscopy of mouse brain tissue. (**A**) Volume rendering of a portion of hippocampus showing neurons (expressing YFP, shown in green) and synapses [marked with anti-Bassoon (blue) and antibody to Homer1 (red)]. (**B**) Volume rendering of dendrites in CA1 slm. (**C**) Volume rendering of dendritic branch in CA1 slm. (**D**) Mossy fiber bouton in hilus of the dentate gyrus. (i) to (iii), selected *z*-slices. Scale bars, (A) 100 μm in each dimension; (B) 52.7 μm (*x*); 42.5 μm (*y*); and 35.2 μm (*z*); (C) 13.5 μm (*x*); 7.3 μm (*y*); and 2.8 μm (*z*); (D), (i) to (iii) 1 μm.

IPR2024-00526
EX 1085

Downloaded from https://www.science.org on March 15, 2025

sample is physically larger, any mechanical errors in post-expansion sectioning, or stage drift, are divided by the expansion factor.

The performance of ExM suggests that despite statistical fluctuations in polymer chain length at the molecular scale, at the nanoscale distances here examined these fluctuations average out, yielding isotropy. Estimates of mesh size for comparable gels suggest that the distance between nearest-neighbor polymer chains are in the ~1 to 2 nm range (*17*, *18*). By tuning the material properties of the ExM polymer, such as the density of cross-links, yet higher effective resolutions may be possible.

REFERENCES AND NOTES

1. T. Tanaka *et al.*, *Phys. Rev. Lett.* **45**, 1636–1639 (1980).
2. I. Ohmine, *J. Chem. Phys.* **77**, 5725 (1982).
3. F. L. Buchholz, *Superabsorbent Polymers* **573**, 27–38 (1994).
4. B. Huang, S. A. Jones, B. Brandenburg, X. Zhuang, *Nat. Methods* **5**, 1047–1052 (2008).
5. E. H. Rego *et al.*, *Proc. Natl. Acad. Sci. U.S.A.* **109**, E135–E143 (2012).
6. M. Bates, B. Huang, G. T. Dempsey, X. Zhuang, *Science* **317**, 1749–1753 (2007).
7. N. Olivier, D. Keller, P. Gönczy, S. Manley, *PLOS One* **8**, (2013).
8. R. W. Cole, T. Jinadasa, C. M. Brown, *Nat. Protoc.* **6**, 1929–1941 (2011).
9. G. Feng *et al.*, *Neuron* **28**, 41–51 (2000).
10. A. Dani, B. Huang, J. Bergan, C. Dulac, X. Zhuang, *Neuron* **68**, 843–856 (2010).
11. A. Rollenhagen, J. H. R. Lübke, *Front. Synaptic Neurosci.* **2**, 2 (2010).
12. G. R. Newman, B. Jasani, E. D. Williams, *Histochem. J.* **15**, 543–555 (1983).
13. K. D. Micheva, S. J. Smith, *Neuron* **55**, 25–36 (2007).
14. B.-C. Chen *et al.*, *Science* **346**, 1257998 (2014).
15. J. Huisken, J. Swoger, F. Del Bene, J. Wittbrodt, E. H. K. Stelzer, *Science* **305**, 1007–1009 (2004).
16. J. H. Lee *et al.*, *Science* **343**, 1360–1363 (2014).
17. A. M. Hecht, R. Duplessix, E. Geissler, *Macromolecules* **18**, 2167–2173 (1985).
18. D. Calvet, J. Y. Wong, S. Giasson, *Macromolecules* **37**, 7762–7771 (2004).

ACKNOWLEDGMENTS

E.S.B. was funded by NIH Director's Pioneer Award 1DP1NS087724 and NIH Director's Transformative Research Award 1R01MH103910-01, the New York Stem Cell Foundation-Robertson Investigator Award, the MIT Center for Brains, Minds, and Machines NSF CCF-1231216, Jeremy and Joyce Wertheimer, Google, NSF CAREER Award CBET 1053233, the MIT Synthetic Intelligence Project, the MIT Media Lab, the MIT McGovern Institute, and the MIT Neurotechnology Fund. F.C. was funded by an NSF Graduate Fellowship. P.W.T. was funded by a Fannie and John Hertz Graduate Fellowship. Confocal imaging was performed in the W. M. Keck Facility for Biological Imaging at the Whitehead Institute for Biomedical Research. Deltavision OMX SR-SIM imaging was performed at the Koch Institute Swanson Biotechnology Center imaging core. We acknowledge W. Salmon and E. Vasile for assistance with confocal and SR-SIM imaging. We acknowledge N. Pak for assistance with perfusions. We also acknowledge, for helpful discussions, B. Chow, A. Marblestone, G. Church, P. So, S. Manalis, J.-B. Chang, J. Enriquez, I. Gupta, M. Kardar, and A. Wissner-Gross. The authors have applied for a patent on the technology, assigned to MIT (U.S. Provisional Application 61943035). The order of co–first author names was determined by a coin toss. The imaging and other data reported in the paper are hosted by MIT (http://expansionmicroscopy.org/rawdataScience2014).

SUPPLEMENTARY MATERIALS

www.sciencemag.org/content/347/6221/543/suppl/DC1
Materials and Methods
Figs. S1 to S5
Tables S1 to S4
References (*19*–*28*)
Movies S1 to S3

18 August 2014; accepted 26 November 2014
10.1126/science.1260088

MITOCHONDRIAL BIOLOGY

Replication-transcription switch in human mitochondria

Karen Agaronyan, Yaroslav I. Morozov, Michael Anikin, Dmitry Temiakov*

Coordinated replication and expression of the mitochondrial genome is critical for metabolically active cells during various stages of development. However, it is not known whether replication and transcription can occur simultaneously without interfering with each other and whether mitochondrial DNA copy number can be regulated by the transcription machinery. We found that interaction of human transcription elongation factor TEFM with mitochondrial RNA polymerase and nascent transcript prevents the generation of replication primers and increases transcription processivity and thereby serves as a molecular switch between replication and transcription, which appear to be mutually exclusive processes in mitochondria. TEFM may allow mitochondria to increase transcription rates and, as a consequence, respiration and adenosine triphosphate production without the need to replicate mitochondrial DNA, as has been observed during spermatogenesis and the early stages of embryogenesis.

The maternally inherited circular mitochondrial DNA (mtDNA) encodes subunits of complexes of the oxidative phosphorylation chain, as well as transfer RNAs (tRNAs) and ribosomal RNAs (*1*, *2*). Transcription of human mtDNA is directed by two promoters, the LSP (light-strand promoter) and the HSP (heavy-strand promoter) located in opposing mtDNA strands, which results in two almost-genome-sized polycistronic transcripts that undergo extensive processing before polyadenylation and translation (*3*, *4*). Note that transcription terminates prematurely about 120 base pairs (bp) downstream of LSP at a vertebrate-conserved G-rich region, called conserved sequence block II (CSBII), as a result of formation of a hybrid G-quadruplex between nascent RNA and the nontemplate strand of DNA (*5*–*7*). This termination event occurs near the origin of replication of the heavy strand (oriH) (*8*) and generates a replication primer. According to the asymmetric model (*9*), replication then proceeds through about two-thirds of the mtDNA, until the oriL sequence in the opposing strand becomes single stranded and forms a hairpin structure. The oriL hairpin is then recognized by mitochondrial RNA polymerase (mtRNAP), which primes replication of the light strand (*10*). Because replication of mtDNA coincides with transcription in time and space, collisions between transcription and replication machineries are inevitable and, similarly to bacterial and eukaryotic systems, likely have detrimental effects on mtDNA gene expression (*11*).

We analyzed the effects of a mitochondrial transcription elongation factor, TEFM, recently described by Minczuk and colleagues (*12*), on transcription of mtDNA. This protein was pulled down from mitochondrial lysates via mtRNAP and was found to stimulate nonspecific transcription on promoterless DNA; however, its effect on promoter-driven transcription had not been determined (*12*). We found that in the presence of TEFM, mtRNAP efficiently transcribes through CSBII (Fig. 1, A and B). Thus, TEFM acts as a factor that prevents termination at CSBII and synthesis of a primer for mtDNA polymerase. We identified the exact location of the termination point in CSBII (fig. S1). MtRNAP terminates at the end of a U6 sequence (positions 287 to 283 in mtDNA), 16 to 18 nucleotides (nt) downstream of the G-quadruplex (Fig. 1A). At this point, the 9-bp RNA-DNA hybrid in the elongation complex (EC) is extremely weak, as it is composed of only A-U and T-A pairs. This is reminiscent of intrinsic termination signals in prokaryotes—where the formation of an RNA hairpin is thought to disrupt the upstream region of the RNA-DNA hybrid—and is followed by the run of six to eight uridine 5′-monophosphate residues that further destabilizes the complex (*5*, *13*).

Human mtDNA is highly polymorphic in the CSBII region; coincidently, the reference mitochondrial genome (Cambridge) contains a rare polymorphism in the G-quadruplex—namely, G5AG7—whereas the majority of mtDNAs from various haplogroups have two additional G residues (G6AG8) (*14*). We found that the termination efficiency of mtRNAP was substantially lower at G5AG7-CSBII (Fig. 1C), which suggested an effect of G run length on quadruplex formation and underscored the importance of further studies of various polymorphisms in this region.

In considering a putative mechanism of TEFM antitermination activity, we investigated whether it can interact with the nascent transcript and, thus, interfere with the formation of the quadruplex structure. We assembled ECs on a nucleic acid scaffold containing a photoreactive analog of uridine, 4-thio-uridine, 13 nt downstream from the 3′ end of RNA, and walked mtRNAP along the template by incorporation of appropriate substrate nucleoside triphosphates (NTPs) (Fig. 2A). We observed efficient cross-linking between TEFM and RNA when the photoreactive base was 15 to 16 bp away from the 3′ end of RNA. Additionally, using a template DNA containing the LSP promoter and

Department of Cell Biology, School of Osteopathic Medicine, Rowan University, 2 Medical Center Drive, Stratford, NJ 08084, USA.
*Corresponding author. E-mail:temiakdm@rowan.edu

Downloaded from https://www.science.org on March 15, 2025

IPR2024-00526
EX 1085